scientific reports

Check for updates

OPEN

Salidroside ameliorates diabetic amyotrophy by targeting Caspase-3 to inhibit apoptosis

Hejie Wang[1,4,5,6], Wafa Yousaf[2,6], Abdul Haseeb[2], Ziyang Wang[3] & Jiangang Zheng[1,4,5]✉

In this study, the Streptozotocin (STZ)-induced diabetes model in rats was employed to assess and verify the activity of salidroside (SAL) in ameliorating diabetic amyotrophy (DA). Network pharmacology analysis was used to obtain SDS-related targets, DA-related targets, and their intersectional targets. After subjecting the targets to GO enrichment and KEGG pathway analysis, a network "target pathway for SAL in ameliorating DA" was set up. Next, the Schrodinger Maestro 13.5 software was utilized for molecular docking to ascertain the binding free energy and binding mode between SAL and target proteins. Molecular dynamics simulations were performed using the Desmond program. Saturation mutation analysis was performed using Schrodinger's Maestro 13.5 software. SPR technology was used to explore the affinity between SAL and Caspase-3 protein. The expression level of Cleaved-Caspase-8, Caspase-8 p18, Cleaved-Caspase-3, Caspase-3 p17, PARP, and PARP P85 proteins in gastrocnemius tissue were determined by Western blotting (WB) analysis. In an STZ-induced rat diabetic model, SAL treatment significantly ($P < 0.05$) reduced blood glucose levels and increased forepaw force. HE and Masson staining results indicated that SAL treatment could significantly increase the mean muscle fiber area ($P < 0.01$) and decrease fibrosis ($P < 0.05$). Immunohistochemical results revealed that SAL treatment significantly increased ($P < 0.01$) the expression of Myogenin and decreased ($P < 0.001$) the expression of FBXO32 in gastrocnemius muscle tissue. Network pharmacological analysis identified that there were a total of 61 intersection proteins, among which TNF, APP, Caspase-3, PPARG, NQO1, HDAC1, BCL2, SRC, HDAC6, ACE, MAPK3, HSP90AA1, ATM, and REN emerged as potential core targets for SAL to ameliorate DA. Based on the crystal structure of the potential core protein, the complex structure model of the core target-SAL was created using molecular docking (XP mode of flexible docking), and the MMGBS analysis was carried out. The SPR results data demonstrated specific binding and kinetic compatibility between the SAL and Caspase-3 proteins. The results of WB revealed that compared with the model group, SAL significantly decreased ($P < 0.05$) expression of Cleaved Caspase-3, Caspase-3 p17, and PARP P85, and significantly increased ($P < 0.05$) the expression of PARP1, while the expression of Cleaved Caspase-8 and Caspase-8 p18 remained unchanged. These results suggest that Caspase-3 is a potential target for SAL to ameliorate DA which eventually plays a role in ameliorating DA by regulating apoptosis-related pathways, which provides a theoretical basis along with clues for the research and development of SAL as ameliorating DA drugs.

Keywords Salidroside, Diabetic amyotrophy, Network pharmacology, Computational biology, Apoptosis, Caspase-3

According to the latest research published by the International Diabetes Federation, the global prevalence of diabetes in 2021 was about 10.5%, ultimately affecting a population of 537 million adults[1]. The findings from the diabetes survey conducted among the population of the Chinese mainland indicate that almost 50% of adults exhibit abnormal blood glucose levels[2]. Currently, the worldwide occurrence of diabetes is progressively

[1]Department of Public Health and Preventive Medicine, Changzhi Medical College, Changzhi 046000, Shanxi, People's Republic of China. [2]College of Veterinary Medicine, Shanxi Agricultural University, Taigu 030801, Shanxi, People's Republic of China. [3]Institute of TCM, Xinjiang Medical University, Urumqi 830000, Xinjiang, People's Republic of China. [4]Shanxi Higher Education Institutions of Science and Technology Innovation Plan Platform, Laboratory of Environmental Factors and Population Health, Changzhi 046000, China. [5]Key Laboratory of Environmental Pathogenic Mechanisms and Prevention of Chronic Diseases, Changzhi Medical College, Changzhi 046000, China. [6]Hejie Wang and Wafa Yousaf: Contributed equally to this work. ✉email: 1349131594@qq.com

rising each year. However, the rates of screening, treatment, and control for diabetes are not optimal. As a result, diabetes has emerged as the leading cause of mortality globally and is imposing an escalating burden on global health. The molecular mechanisms underlying diabetes complications are highly intricate, and most contemporary studies mainly focus on cardiovascular disease, blindness, and renal failure complications in diabetes patients. Nevertheless, there is a scarcity of studies investigating diabetic amyotrophy[3].

The syndrome was first characterized by German neuropathologist Bruns in 1890. Garland coined the term "diabetic muscular dystrophy" in the 1950s. DA initially manifests as unilateral pain in the thigh or hip, subsequently radiating to the contralateral leg due to lesions affecting the lumbosacral roots, nerve plexus, and peripheral nerves, ultimately resulting in muscle atrophy and weight loss[4]. Feng et al. showed that the overall prevalence rate of diabetic muscular atrophy patients across different age categories was about 18%, among which the elderly were high-risk groups. As human life expectancy continues to increase as society ages, DA poses an escalating threat to human health[5]. At present, DA can only be prevented by blood glucose level control, and there is no specific drug, so the development of drugs is imminent.

According to the Chinese medical book *Modern Practical Materia Medica*, Rhodiola Rosea possesses therapeutic properties to treat diabetes in the elderly age and has the effect of inhibiting the rise of blood glucose. Its primary constituent SAL has the attributes of nerve repair and regeneration, anti-oxidation, and anti-muscular atrophy[6–8]. One of the causes of diabetic muscular atrophy is inadequate perineuronal microcirculation which leads to hypoxia, insufficient nutrient supply, and ROS accumulation of nerve cells leading to peripheral nerve injury and thus aggravating skeletal muscle atrophy[9]. SAL can mitigate skeletal muscle atrophy by improving peripheral nerve injury[10]. In conclusion, SAL possesses great potential to ameliorate DA.

In this study, an STZ-induced diabetic rat model was used to assess the activity and efficacy of SAL in ameliorating diabetic muscular atrophy, but its target and specific mechanism are not clear. The advancement of bioinformation technologies such as network pharmacology, molecular docking, and molecular dynamics simulation have made clinical trials obsolete for drug screening and development. The utilization of the aforementioned techniques enables the anticipation of drug targets, elucidation of ligand-target interactions at the molecular level, and simulation of the ligand-target time evolution process. This approach can significantly streamline the screening process by reducing the necessity for extensive experimentation[11–14]. Therefore, in this study, network pharmacology, molecular docking, molecular dynamics simulation, and WB techniques were employed to analyze the key targets and associated mechanisms of SAL in ameliorating DA and to evaluate the potential of SAL as a drug for ameliorating DA.

Results

Effects of salidroside on diabetic amyotrophy in STZ-induced diabetic rat

To evaluate the activity of salidroside in ameliorating diabetic amyotrophy, STZ-induced diabetic rat models were used in this study. Compared with the control group, body weight and forepaw strength were significantly decreased ($P<0.05$) whereas blood glucose level was significantly increased ($P<0.05$) after STZ induction for 2 weeks (Fig. 1A–C). After 3–4 weeks of salidroside treatment, the blood glucose of diabetic rats could be significantly ($P<0.05$) reduced. After 4 weeks of salidroside treatment, the weight and front paw force of diabetic rats could be significantly ($P<0.05$) improved (Fig. 1A–C). The results of histopathological sections showed that vacuolated lesions and increased muscle fiber spaces (White arrow) occurred in the muscles of the model group,

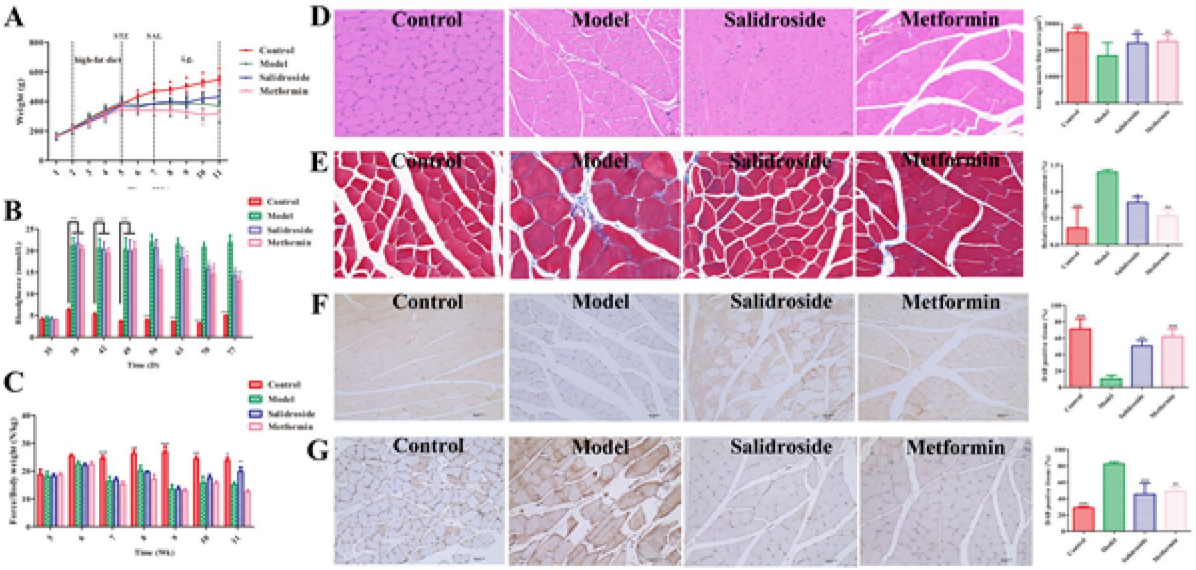

Fig. 1. Effects of salidroside on diabetic amyotrophy in STZ-induced diabetic rats. (**A**) Body weight. (**B**) Blood glucose. (**C**) Front paw force. (**D**) H&E staining of gastrocnemius muscle after 4 weeks of salidroside treatment. (**E**) Masson staining of gastrocnemius muscle after 4 weeks of salidroside treatment. (**F** and **G**) The expression of MyoG and FBXO32 proteins was detected by IHC, respectively, after 4 weeks of salidroside treatment.

while salidroside could alleviate these symptoms (Fig. 1D). Compared with the control group, the average area of muscle fibers (Black arrow) in the model group was significantly ($P<0.001$) reduced (Fig. 1D), and there were a lot of vacuolation lesions (Red arrow) and inconsistency of muscle fiber size, while the collagen content (Blue arrow) was significantly ($P<0.001$) increased (Fig. 1E). After 4 weeks of salidroside treatment, this condition can be significantly ($P<0.05$) improved. The IHC results showed that compared with the control group, the expression level of MyoG was significantly ($P<0.001$) decreased in the model group, while the expression level of FBXO32 was significantly ($P<0.001$) increased, which could be reversed after 4 weeks of salidroside treatment ($P<0.001$, Fig. 1F and G).

Network pharmacology predicts the targets of SAL effect on DA

Through *ChEmBL* and *GeneCards* databases, 2219 salidroside action targets and 315 DA-related targets were collected respectively, with the target species characterized as human. The targets collected above were intersected and the protein obtained was identified as a viable potential target of SAL for ameliorating DA. The targets of SAL for ameliorating DA were visualized by the Venn diagram and the results are shown in Fig. 2A. There were a total of 61 intersection proteins, as presented in Table 1.

The 61 intersection targets obtained were imported into the *STRING* database to obtain the protein interaction network diagram (Fig. 2B). The tsv files of intersection targets were imported into Cytoscape v3.9.1 and the core targets with higher than average node connectivity (62.60), average node interconnectivity (0.50), and average node closeness (12.46) were selected by CytoNCA plug-in to draw the Hithubs network (Fig. 2C). Results demonstrated that the core targets of salidroside in ameliorating DA are TNF, CASP3, PPARG, BCL2, APP, MAPK3, SRC, HSP90AA1, HDAC1, ACE, ATM, REN, HDAC6, and NQO1.

61 potential targets of SAL for ameliorating DA were input into the *DAVID* database for GO function and KEGG pathway enrichment analysis. A total of 351 GO and 105 KEGG enrichment results were obtained. Among them, 240 biological processes were involved, which were mainly related to the regulation of the apoptosis process, stress response, and neuronal apoptosis process. There were 53 cell components, which were mainly related to mitochondria, neuron cells, membrane channels, and their related proteins. There were 58 molecular functions, which were mainly related to enzyme activity and protein binding (Fig. 2D). The KEGG was mainly associated with lipid and atherosclerosis, apoptosis, and a variety of neurodegenerative disease pathways (Fig. 2E). Enrichment analysis for GO functions and KEGG pathways was conducted, yielding p-values for the top 20 significant results, which were shown using a column type and bubble chart on the online mapping platform (http://www.bioinformatics.com.cn/). According to the results, the effect of SAL on DA may be related to the regulation of apoptosis and neurotransmission.

Cytoscape 3.9.1 software was employed to integrate the 14 core targets of salidroside for ameliorating DA and identifying the top 20 pathways enriched with *P*-value. Subsequently, a salidroside-target-pathway network was constructed (Fig. 2F). The nodes in the network diagram represent TCM monomers, target proteins, and pathways respectively, and the edges represent the interactions between drug molecules and specific proteins and pathways. There were 288 pairs of protein-pathway relationships. The network diagram indicated that salidroside could play a role in anti-apoptosis and repair nerve damage by regulating pathway-related target proteins.

Molecular docking study

SAL was connected to the surfaces of TNF, APP, Caspase-3, PPARγ, NQO1, HDAC1, BCL2, SRC, HDAC6, ACE, MAPK3, HSP90AA1, ATM, and REN active pockets, respectively. SAL generated hydrophobic forces with Caspase-3 residues TYR204 and PHE256, created a hydrogen bond with HIE121, and established two hydrogen bonds with ARG207 (Fig. 3A). SAL generated a hydrophobic force with residues PRO103 and PHE107 of NQO1, and established a hydrogen bond with residues ASN19, GLY150, GLY151 and TRP106 respectively (Fig. 3B). SAL generated hydrophobic forces with residues TRP45, VAL111, MET114, VAL88, and LEU81 of REN, and established hydrogen bonds with residues ASP38, GLY228, and TYR83 (Fig. 3C). SAL generated a hydrophobic force with residues PHE620 and LEU749 of HDAC6, and established a hydrogen bond with residues LEU749, HIE651 and HIS610 (Fig. 3D). SAL generated a hydrophobic force with ACE residue VAL380, formed a hydrogen bond with residues HIE513, HIE353 and GLN281, and established two hydrogen bonds with residues GLU384 (Fig. 3E). SAL generated a hydrophobic force with residues PHE138, VAL150 and LEU48 of HSP90AA1, and established a hydrogen bond with residues ASN51 and ASP93 (Fig. 3F). SAL generated hydrophobic forces with residues ILE101, CYS183, TYR53, ALA69, and LEU173 of MAPK3, and established hydrogen bonds with residues LYS131, GLU126, and GLN122 (Fig. 3G). SAL generated a hydrophobic force with residues ILE262, PHE264, CYS285, VAL339, and ILE341 of PPARγ, and established a hydrogen bond with residues SER342 and ARG280 (Fig. 3H). SAL generated a hydrophobic force with BCL2 residues ALA149, PHE150, PHE153, and VAL133, and established a hydrogen bond with residues ALA149 and GLY145 (Fig. 3I). SAL generated hydrophobic forces with SRC residues MET341, TYR340, and LEU273, and established two hydrogen bonds with residue MET341 (Fig. 3J). SAL generated hydrophobic forces with residues TYR151 and VAL150 of TNF, formed a hydrogen bond with residues ALA18, SER147, and GLY148, and established two hydrogen bonds with residues VAL150 (Fig. 3K). SAL generated hydrophobic forces with residues VAL461 and ALA384 of APP and established one hydrogen bond with residues ALA384, ARG394, and ARG395, and two hydrogen bonds with residues ASN391 (Fig. 3L). SAL generated a hydrophobic force with residues PHE107, LEU106, and PHE103 of HDAC1, and established a hydrogen bond with residues GLN111 and ILE79 respectively (Fig. 3M). In addition, SAL cannot bind to ATM protein.

As shown in the results of XP (Table 2) and MM-GBSA energy (Table 3, Fig. 3N), the score of SAL with Caspase-3 was −10.769, and the results of MM-GBSA energy was −47.34. The low binding free energy and docking scores indicate that SAL has strong binding stability with Caspase-3. SAL has low binding free energy

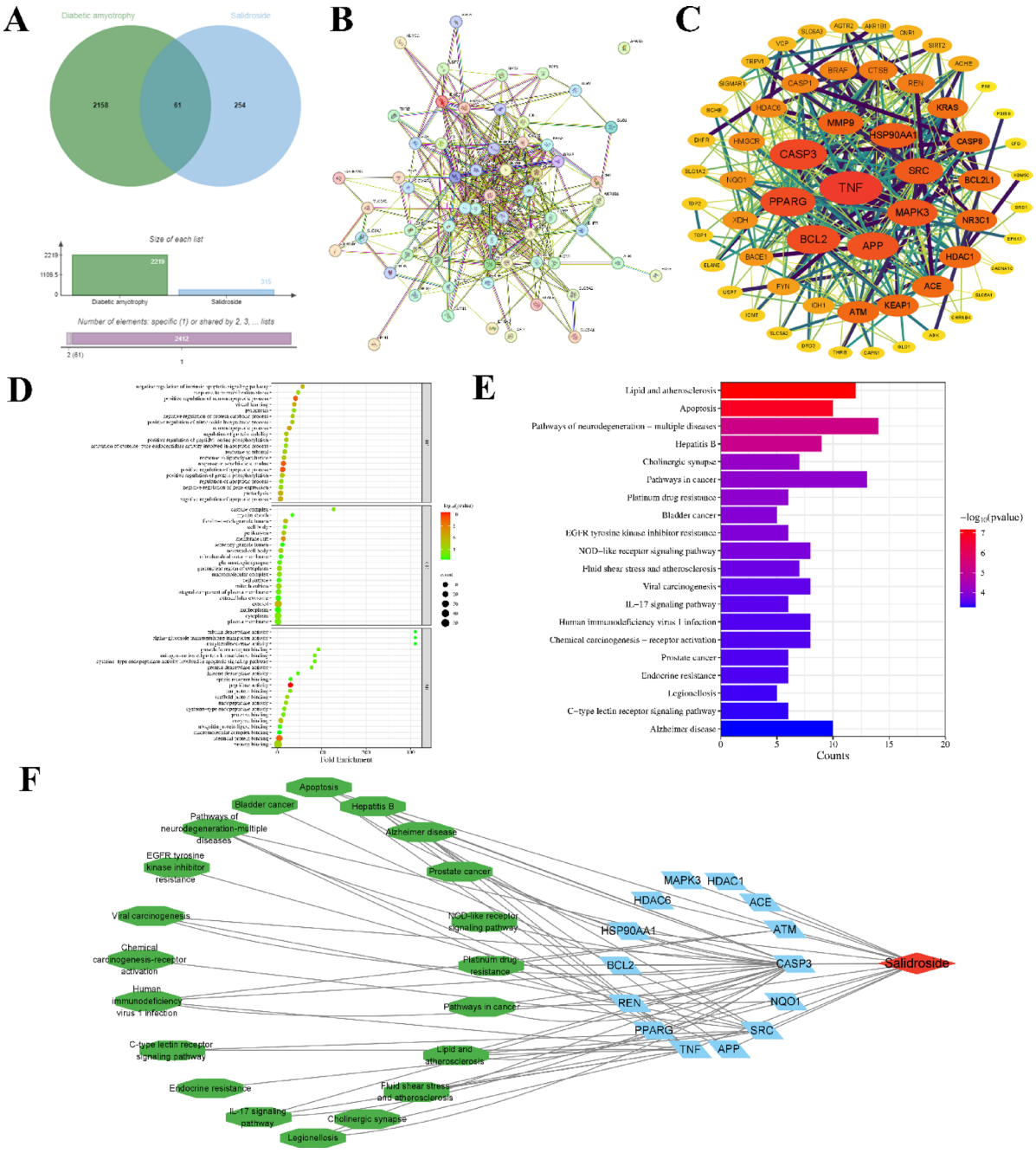

Fig. 2. Network pharmacology predicts the target of salidroside relieving DA. (**A**) Venn diagram of potential targets of salidroside in ameliorating DA. (**B** and **C**) Salidroside ameliorates DA potential targets PPI network and Hithubs network. (**D**) The target that was enriched by the Gene Ontology of SAL in ameliorating DA. (**E**) The target was enriched by the KEGG Pathway of SAL in ameliorating DA. (**F**) SAL-target-pathway network model.

with NQO1, HSP90AA1, PPARγ, BCL2, SRC, and TNF, and a low binding score, indicating that SAL binds to these 6 proteins stably. In addition, SAL had high binding free energy with REN, HDAC6, ACE, MAPK3, APP, and HDAC1, indicating that the binding of SAL to these 6 proteins was unstable.

MD simulations and key binding sites saturated mutation affinity results

The 100 ns MD simulation of SAL and Caspase-3 protein was performed, and their molecular dynamics trajectory was analyzed. The results revealed that SAL and Caspase-3 proteins were relatively stable after 60 ns and the system was in a state of equilibrium (Fig. 4A). After SAL binding to Caspase-3 protein, the protein showed high structural flexibility in the 140-170AA residue region (Fig. 4B). Protein–ligand interactions could be monitored throughout the simulation. The principal amino acids that played a significant role in the binding

Serial number	Gene symbol	Uniprot ID	Protein name
1	PPARG	P37231	Peroxisome proliferator-activated receptor gamma
2	ACE	P12821	Angiotensin-converting enzyme
3	TNF	A0A0G2YPN5	Tumor necrosis factor
4	AKR1B1	P15121	Aldo–keto reductase family 1 member B1
5	ATM	Q13315	Serine-protein kinase ATM
6	SLC5A2	P31639	Sodium/glucose cotransporter 2
7	MMP9	P14780	Matrix metalloproteinase-9
8	REN	P00797	Renin
9	NR3C1	P04150	Glucocorticoid receptor
10	HMGCR	P04035	3-hydroxy-3-methylglutaryl-coenzyme A reductase
11	GPR35	Q9HC97	G-protein coupled receptor 35
12	VCP	P55072	Valosin-Containing Protein
13	CNR1	P21554	Cannabinoid receptor 1
14	BRAF	P15056	Serine/threonine-protein kinase B-raf
15	SLC5A1	P13866	Sodium/glucose cotransporter 1
16	AGTR2	P50052	Type-2 angiotensin II receptor
17	GLO1	Q04760	Lactoylglutathione lyase
18	BCHE	P06276	Cholinesterase
19	ACHE	P22303	Acetylcholinesterase
20	CASP3	P42574	Caspase-3
21	CTSB	P07858	Cathepsin B
22	HSP90AA1	P07900	Heat shock protein HSP 90-alpha
23	SRC	P12931	Proto-oncogene tyrosine-protein kinase Src
24	BCL2	P10415	Apoptosis regulator Bcl-2
25	XDH	P47989	Xanthine dehydrogenase/oxidase
26	APP	P05067	Amyloid-beta precursor protein
27	TRPV1	Q8NER1	Transient receptor potential cation channel subfamily V member 1
28	KRAS	P01116	GTPase KRas
29	NQO1	P15559	NAD(P)H dehydrogenase quinone 1
30	CAPN1	P07384	Calpain-1 catalytic subunit
31	CACNA1C	Q13936	Voltage-dependent L-type calcium channel subunit alpha-1C
32	CASP1	P29466	Caspase-1
33	KEAP1	Q14145	Kelch-like ECH-associated protein 1
34	THRB	P10828	Thyroid hormone receptor beta
35	CASP8	Q14790	Caspase-8
36	SIGMAR1	Q99720	Sigma non-opioid intracellular receptor 1
37	EPHX1	P07099	Epoxide hydrolase 1
38	MAPK3	L7RXH5	Mitogen-activated protein kinase
39	PDE8B	O95263	High affinity cAMP-specific and IBMX-insensitive 3',5'-cyclic phosphodiesterase 8B
40	ELANE	P08246	Neutrophil elastase
41	TDP2	O95551	Tyrosyl-DNA phosphodiesterase 2
42	HDAC6	Q9UBN7	Histone deacetylase 6
43	CFD	P00746	Complement factor D
44	BCL2L1	Q07817	Bcl-2-like protein 1
45	CHRNB4	P30926	Neuronal acetylcholine receptor subunit beta-4
46	BACE1	P56817	Beta-secretase 1
47	IDH1	O75874	Isocitrate dehydrogenase [NADP] cytoplasmic
48	DRD3	P35462	D(3) dopamine receptor
49	HDAC1	Q13547	Histone deacetylase 1
50	SIRT2	Q8IXJ6	NAD-dependent protein deacetylase sirtuin-2
51	KDM5C	P41229	Lysine-specific demethylase 5C
52	SLC6A3	Q01959	Sodium-dependent dopamine transporter
53	SLC1A2	P43004	Excitatory amino acid transporter 2
54	DHFR	P00374	Dihydrofolate reductase
55	FYN	P06241	Tyrosine-protein kinase Fyn
56	ADK	P55263	Adenosine kinase

Continued

Serial number	Gene symbol	Uniprot ID	Protein name
57	TOP1	P11387	DNA topoisomerase 1
58	USP7	Q93009	Ubiquitin carboxyl-terminal hydrolase 7
59	PIN1	Q13526	Peptidyl-prolyl cis–trans isomerase NIMA-interacting 1
60	ICMT	O60725	Protein-S-isoprenylcysteine O-methyltransferase
61	BRD1	O95696	Bromodomain-containing protein 1

Table 1. Targets of salidroside for alleviating diabetic amyotrophy.

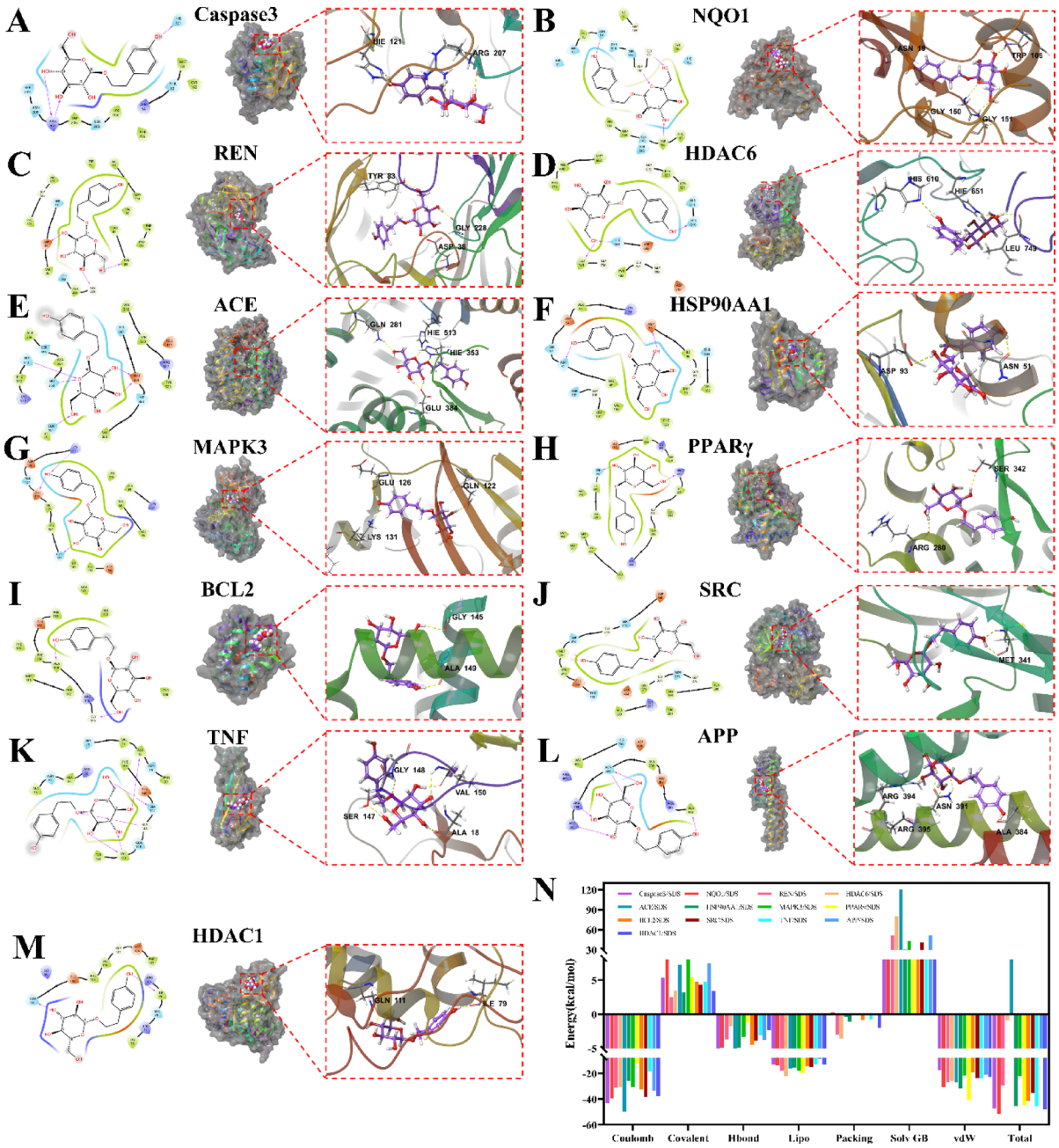

Fig. 3. Molecular docking predicts the binding activity of SAL to the target. Molecular docking complexes of SAL with Caspase-3 (**A**), NQO1 (**B**), REN (**C**), HDAC6 (**D**), ACE (**E**), HSP90AA1 (**F**), MAPK3 (**G**), PPARγ (**H**), BCL2 (**I**), SRC (**J**), TNF (**K**), APP (**L**) and HDAC1 (**M**) (Yellow represents hydrogen bonds, and green represents π-Cation bonds). (**N**) Statistical diagram of the MM/GBSA calculation for the complexes.

Compound	Target	XP Gscore
Salidroside	Caspase3	− 10.769
	NQO1	− 10.401
	REN	− 10.273
	HDAC6	− 9.290
	ACE	− 9.281
	HSP90AA1	− 8.864
	MAPK3	− 8.824
	PPARγ	− 8.742
	BCL2	− 8.718
	SRC	− 8.604
	TNF	− 7.757
	APP	− 6.055
	HDAC1	− 5.390
	ATM	NA

Table 2. XP docking score of core target with salidroside.

	Caspase3	NQO1	REN	HDAC6	ACE	HSP90AA1	MAPK3	PPARγ	BCL2	SRC	TNF	APP	HDAC1
Energy	Salidroside												
Coulomb	− 42.98	− 39.37	− 31.12	− 30.66	− 49.91	− 25.83	− 30.53	− 12.47	− 32.61	− 38.30	− 18.50	− 33.35	− 37.85
Covalent	5.35	8.45	2.47	3.45	7.20	3.18	8.03	5.46	4.76	4.35	4.80	7.50	3.39
Hbond	− 7.01	− 4.88	− 3.69	− 1.76	− 5.73	− 4.91	− 3.37	− 1.25	− 4.44	− 3.86	− 3.13	− 3.76	− 2.36
Lipo	− 13.20	− 14.00	− 18.24	− 22.42	− 16.25	− 15.43	− 17.80	− 19.83	− 14.44	− 14.92	− 13.18	− 8.82	− 13.19
Packing	− 0.23	− 0.05	− 3.03	− 3.57	− 0.45	− 1.12	0.00	0.00	− 0.87	− 0.00	− 0.77	− 0.00	− 2.01
Solv GB	28.15	29.17	51.05	79.77	120.02	30.76	43.03	23.53	25.51	41.31	9.13	51.98	27.11
vdW	− 17.42	− 30.66	− 27.02	− 25.73	− 26.80	− 31.90	− 21.77	− 40.56	− 19.41	− 23.74	− 23.97	− 21.01	− 22.91
Total	− 47.34	− 51.33	− 29.59	− 0.92	28.08	− 45.25	− 22.41	− 45.12	− 41.50	− 35.17	− 45.62	− 7.46	− 47.81

Table 3. Statistical analysis of MM/GBSA results.

of SAL and Caspase-3 protein were TRP206, ASN208, TRP214, and PHE250, and their interactions were mainly water bridge, hydrogen bond, and hydrophobic effect (Fig. 4C). Figure 4D illustrates the temporal variation in the interaction between SAL and particular amino acids of the Caspase-3 protein along the trajectory. The results showed that amino acid residues TYR204, TRP206, ASN208, ASP211, TRP214, GLU246, GLU248, PHE250, SER251, and PHE256 had multiple contacts with SAL (shown in darker orange). The diagram is shown in Fig. 4E. The conformational evolution of each RB in SAL within the entire simulated locus (0–100 ns) is shown in Supplementary Fig. S1.

After saturation mutation of key binding sites, the highest Δaffinity results of Caspase-3 protein were 206 (TRP→GLY), A:206 (TRP→LYS), and A:206 (TRP→ALA), The corresponding values were 10.847 kcal/mol, 10.008 kcal/mol, and 9.725 kcal/mol respectively (Fig. 4F). Among the top10 Δaffinity results for Caspase-3 protein (Table 4), the highest occurrence revealed at site 206 (Fig. 4G). The results of the MM GBSA binding free energy of the affinity mutations at the three sites with the highest Δaffinity results of Caspase-3 protein are shown in Table 5. These mutations significantly weakened the hydrophobic force and van der Waals force generated by the ligand on the protein and inhibited the binding of the ligand to the protein. At the three sites with the highest Δaffinity of Caspase-3 protein, it was difficult to find significant changes in the two-dimensional structure, so it could be indicated that the mutation mainly affected non-covalent bonds such as hydrogen bonds and salt Bridges (Supplementary Fig. S2).

The affinity between salidroside and Caspase-3 protein

SPR biosensor was used to detect the affinity between SAL and Z-DEVD-FMK and Caspase-3 protein. The results showed that the dissociation constant Kd value of SAL and Z-DEVD-FMK was low and the affinity parameters are shown in Table 6. Both SAL (Fig. 5A) and Z-DEVD-FMK (Fig. 5B) have good affinity for the fitting curves produced by reacting with the Caspase-3 protein.

Salidroside inhibits Caspase-3 protease activity independently of Caspase8 protease

The expression of proteins related to the apoptotic pathway was detected by WB. Compared with the control group, STZ induced the significant production of Cleaved Caspase-3, Caspase-3 p17, Cleaved Caspase-8, Caspase-8 p18 and PARP P85 protein (Fig. 5C), and significantly ($P<0.05$) decreased the expression of PARP. Compared with the model group, SAL significantly decreased ($P<0.05$) the expression of Cleaved Caspase-3, Caspase-3

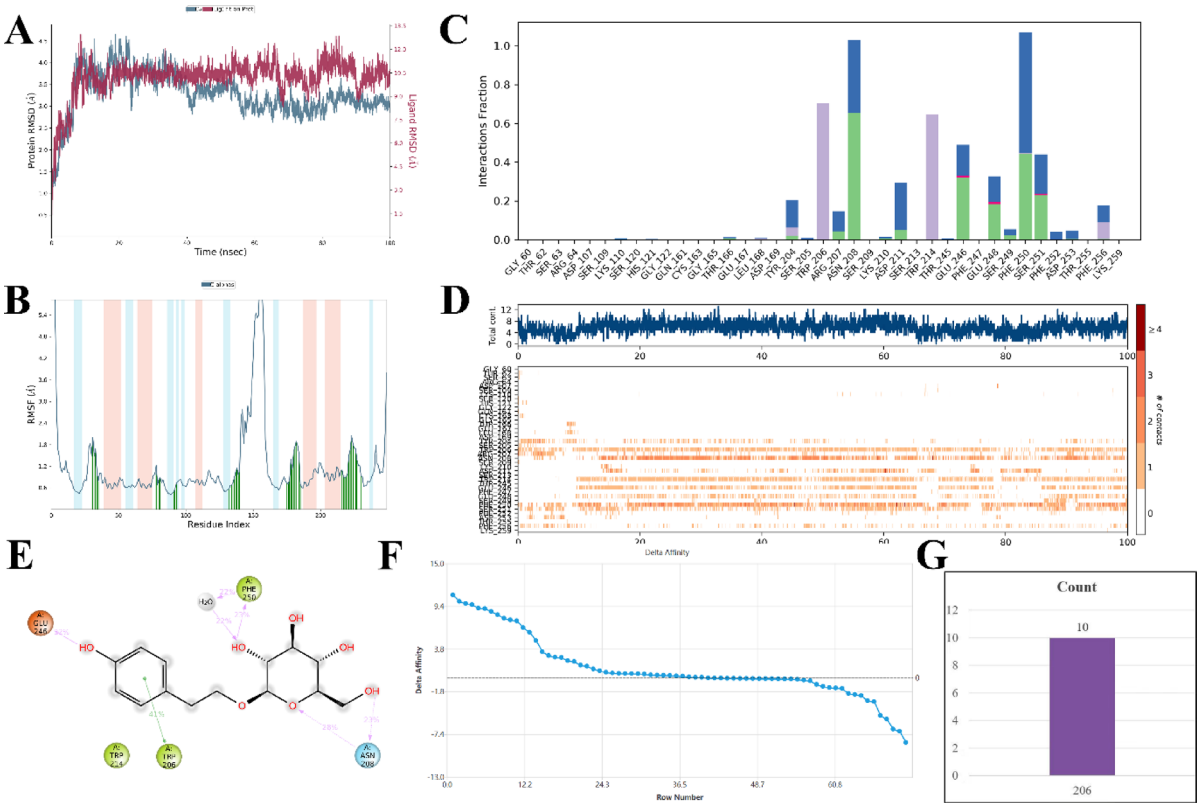

Fig. 4. MD simulation and saturation mutation of key binding sites predicted the binding sites of SAL and Caspase-3. (**A**) is the molecular dynamics simulation -RMSD value (The blue line represents the proteins, and the red line represents salidroside). (**B**) is the molecular dynamics simulation -RMSF value (α-helical and β-strand regions are highlighted in red and blue backgrounds, respectively. Protein residues that interact with the ligand are marked with green-colored vertical bars). (**C**) represents the contribution of amino acids at Caspase-3 binding sites to SAL-protein binding, respectively. (**D**) shows how interactions between SAL and specific amino acids of the Caspase-3 proteins have changed over time, respectively (shown in orange with varying depths, according to the proportions on the right side of the figure). € is a detailed diagram of SAL's interactions with Caspase-3 protein residues. (**F**) Trend diagram of saturation mutagenesis results at key binding sites. (**G**) TOP10 results of saturation mutagenesis affinity of key binding sites.

Caspase-3	
Mutations	**△Affinity (kcal/mol)**
A:206(TRP → GLY)	10.847
A:206(TRP → LYS)	10.008
A:206(TRP → ALA)	9.725
A:206(TRP → ASP)	9.579
A:206(TRP → THR)	9.133
A:206(TRP → SER)	9.068
A:206(TRP → CYS)	8.697
A:206(TRP → PRO)	8.261
A:206(TRP → VAL)	7.797
A:206(TRP → GLU)	7.582

Table 4. TOP10 saturation mutagenesis affinity of key binding sites.

p17, and PARP P85, and significantly increased ($P<0.05$) the expression of PARP1, while the expression of Cleaved Caspase-8 and Caspase-8 p18 remained unchanged. The results indicated that SAL inhibited the activity of Caspase-3 protease independently of Caspase8 protease.

Protein	Title	Δaffinity	Coulomb	Covalent	Hbond	Lipo	Packing	Solv GB	vdW
Caspase3	A:220 (CYS→TRP)	10.847	1.441	−5.727	0.000	5.651	0.109	−1.352	4.999
	A:220(CYS→TYR)	10.008	3.344	1.836	−0.003	5.936	0.109	−1.680	2.302
	A:220 (CYS→PHE)	9.725	41.442	−1.291	0.000	4.860	0.109	−1.270	4.583

Table 5. The change of MM-GBSA binding free energy in saturation mutagenesis affinity TOP3 at key binding sites.

Protein	Ligand	KD (M)	Rmax (RU)
TLR4	Salidroside	7.67×10^{-5}	7.100
	Z-DEVD-FMK	6.42×10^{-5}	5.600

Table 6. Affinity of Caspase-3 protein with Salidroside and Z-DEVD-FMK.

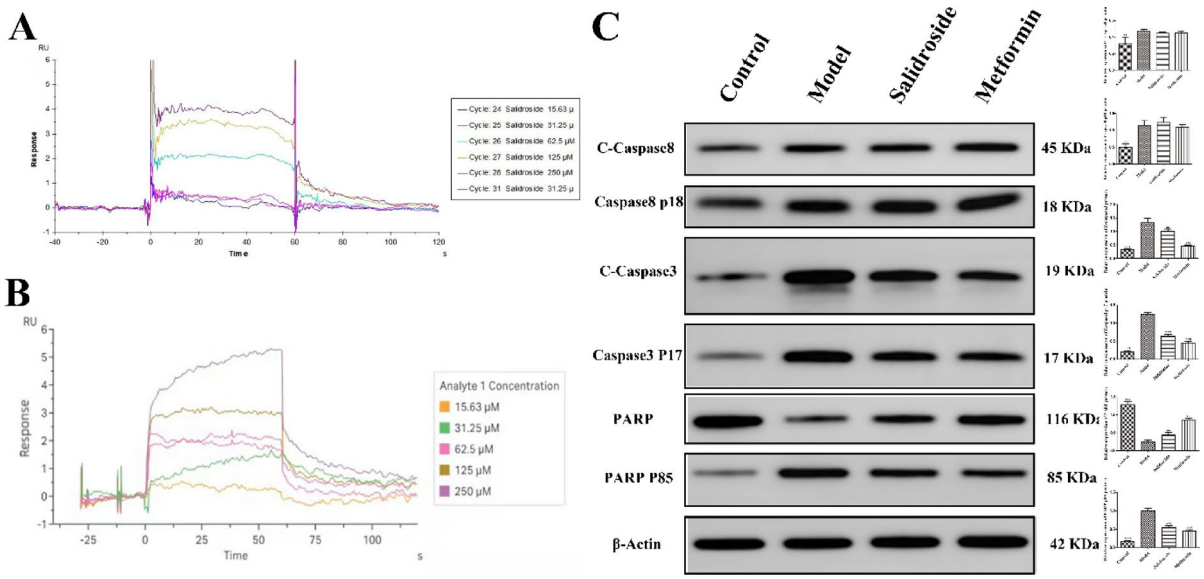

Fig. 5. SAL targeting Caspase-3 inhibits the apoptosis pathway and alleviates DA. Surface plasmon resonance was used to test the affinity of Caspase-3 protein with different concentrations of salidroside (**A**) and Z-DEVD-FMK (**B**). (**C**) The expression of Cleaved-Caspase-8, Caspase-8 p18, Cleaved-Caspase-3, Caspase-3 p17, PARP, and PARP P85 proteins were detected by Western blot. Original blots are presented in Supplementary Fig. S3.

Materials and methods

Compounds, reagents, and antibodies

Salidroside (Cat: HY-N0109), Metformin (Cat: HY-B0627), Streptozotocin (STZ, Cat: HY-13753), and Z-DEVD-FMK (Cat: HY-12466) were purchased from MCE (USA), with 99.79%, 99.98%, 99.15%, and 98% purity, respectively. Recombinant human Caspase-3 protein (Active) was purchased from Abcam (USA).

CM5 Sensor Chip was purchased from Cytiva (USA). 1-Ethyl-3-(3-dimethylaminopropyl) carbodiimide (EDC), N-Hydroxysuccinimide (NHS), and ethanolamine were purchased from Sigma (USA). NaOH 50 mM and sodium acetate solution (pH4.0) were purchased from GE Healthcare (USA).

Anti-PARP1 (Cat: GB11841-100) Rabbit pAb, Anti-PARP1 p85 (Cat: GB11841-101) Rabbit pAb, Anti-beta Actin (Cat: GB15003) Rabbit pAb, and Goat anti-rabbit secondary antibodies (Cat: GB23303) were purchased from Servicebio (China). Anti-Cleaved-Caspase-8 (Cat: AF5267) Rabbit pAb was purchased from Affinity (Australia). Anti-Caspase-8 p18 (Cat: WL00659) Rabbit pAb was purchased from Wanleibio (China). Anti-Cleaved-Caspase-3 (Cat: 9661) Rabbit pAb was purchased from CST (USA). Anti-Caspase-3 P17 (Cat: ab184787) Rabbit pAb was purchased from Abcam (USA). Anti-Myogenin (Cat: PA5-119,967) and FBXO32 (Cat: PA5-106,917) Rabbit pAb were purchased from Thermo Fisher (USA).

Animal modeling and treatment

Four-week-old SD males (weight 100 g) were procured from SPF Biotechnology Co. Ltd (Beijing, China). The number of male rats in each group was equal. The animals were maintained in a controlled environment with a 12-h light/dark cycle, with free access to food and water. All animal experiments were approved by the Ethics

Committee of Changzhi Medical College (DW2024140, July 22, 2024) and were conducted by its guidance and regulations. All animal experiments were followed described by the ARRIVE guidelines (PLoS Bio 8(6), e1000412,2010). After a one-week acclimatization period, the rats were randomly allocated into four groups (n = 8 per group): (1) Control group; (2) Model group, rats were fed a high-sugar and high-fat diet (containing 67% maintenance diet, 10% lard, 20% sucrose, 2.5% cholesterol, 0.5% sodium cholate) over 4 weeks, subsequently fasted for 12 h, and were administered STZ 45 mg/kg by intraperitoneal injection; (3) Treatment group, after 2 weeks of metformin injection, 50 mg/kg SAL was administered by gavage for 4 weeks (salidroside group)[15]; (4) Positive control group, after 2 weeks of metformin injection, 500 mg/kg metformin was administered by gavage for 4 weeks (Metformin group)[16]. The 0.9% saline to dissolve the doses of STZ (9 mg/mL). The volume of 0.5% carboxymethyl cellulose to dissolve the doses of SAL (10 mg/mL) and metformin (100 mg/mL), respectively. The control group and model group were given intraperitoneal injection and oral gavage of 0.9% saline and 0.5% carboxymethyl cellulose equal to the treatment group and positive control group. During the experiment, the body weight, blood glucose, and front paw force of the rats were measured at different intervals of time, followed by the dissection, fixation, and freezing of the gastrocnemius muscle tissue subsequent to euthanasia via CO_2. The parameters of CO_2 euthanasia are as follows: the chamber volume is $50 \times 37 \times 28$ cm, the flow rate is 30% chamber volume/min, the CO_2 concentration gradually increases to 90% of the chamber volume, and the treatment time is 5 min.

Pathological and immunohistochemical analyses

Tissue samples of rat gastrocnemius were fixed with 4% paraformaldehyde solution (Solarbio, China). The fixed tissue was dehydrated by a fully automatic dehydrator (JT-12S, Wuhan Junjie Electronics Co., LTD., China), later trimmed, embedded, and sliced into paraffin sections.

The hematoxylin and eosin (H&E) protocol (Solarbio, China) was performed to visualize pathological changes in gastrocnemius tissue samples. Image acquisition was performed using the Pannoramic 250 digital slice scanner (3DHISTECH, Hungary). Using the Caseviewer software 2.4 (3DHISTECH, Hungary), the Linear measurement annotation measurement tool in annotation was selected to measure the muscle fiber area.

The collagen fibers and muscle fibers pathological changes of gastrocnemius tissue samples were examined by Masson staining. Paraffin sections dewaxed to water; Overnight incubation with potassium dichromate; Heat the slices in the oven at 63 C for 1 h. Ponceau fuchsin staining solution for 10 min, slightly washed with distilled water; Phosphomolybdic acid solution was treated for a few seconds to 2 min until the collagen fiber faded; Aniline blue dyeing about 2 min, collagen fiber color can be; Gradient alcohol dehydration, transparent agent transparent, neutral gum seal. Image acquisition was performed using the Pannoramic 250 digital slice scanner (3DHISTECH, Hungary). Image-Pro Plus 6.0 software (Media Cybernetics, USA) was used to measure the positive expression area in the collected images, and the percentage of positive expression area = positive expression area/visual field area (pixel area).

The expression of MyoG and FBXO32 in gastrocnemius was detected by immunohistochemistry (IHC). Paraffin sections were dewaxed to water, and then treated with antigen repair, endogenous peroxidase blocking, and bovine serum blocking. MyoG and FBXO32 primary antibodies (1:300 and 1:100) were applied, and the sections were placed in a wet box at 4 °C and incubated overnight, and then secondary antibody (HRP labeled goat anti-rabbit, 1:100) was applied. DAB drops were added to the tissue and the color development time was controlled under the microscope, the positive color was brownish yellow, and the color development was terminated by rinsing the section with distilled water. Hematoxylin was re-dyed for 3 min and finally sealed by dehydration. Image acquisition was performed using the Pannoramic 250 digital slice scanner (3DHISTECH, Hungary). The percentage of DAB Positive Tissue in each image was calculated using Halo software.

Network pharmacology

Salidroside and DA-related target screening

Based on previous work and related literature reports, this study used "Salidroside" and "Diabetic amyotrophy" as search terms to gather pertinent targets. Initially, protein structure, Compound CID, MF, and SMILES of SAL were obtained from the *PubChem* database (https://pubchem.ncbi.nlm.nih.gov/)[17]. The SAL target was obtained from *CHEMBL* (https://www.ebi.ac.uk/chembl/) in this study. Finally, DA-related target data were retrieved through the *Gene Cards* database (https://www.gene- cards.org)[18].

Visual analysis of SAL ameliorating DA target and construction of PPI network

The screened SAL-related targets were intersected along with the DA-related targets to map Venny. The data was imported into the Venny platform (https://bioinfogp.cnb.csic.es/tools/Venny/index.HTML), the intersection targets were visualized and the target of SAL ameliorating DA was obtained. Then, the target was imported into the *STRING* database (https://string-db.org/), and the species '*homo–sapiens*' was selected to obtain the interaction relationship of target proteins, and the protein–protein interaction network and tsv files were exported[19]. Subsequently, the tsv file was imported into Cytoscape v3.9.1 to draw the Hithubs network, Network Analyzer was used to conduct topological analysis on the network. Node size and color depth were used to reflect the degree score, and edge thickness was used to reflect the combined score. The core of targets was screened according to the values of degree centralities, betweenness centralities, and closeness centralities.

GO enrichment and KEGG pathway analysis

Data were submitted to the *DAVID v2023q3* database (https://david.ncifcrf.gov/), imported the potential targets of SAL ameliorating DA, selected the species '*homo-sapiens*', set the identifier and listed type to official gene symbol and gene list, respectively[20]. GO function and KEGG pathway enrichment analysis were performed on potential targets of SAL ameliorating DA, and the results were exported to a Txt file. The targets were sorted

according to *P* values, and the top 20 terms in *P* values that were enriched by GO (Biological Process, Molecular Function, and Cellular Component) and KEGG were selected, and they were imported into the online platform (http://www.bioinformatics.com.cn/) draw column chart and bubble chart[21,22].

Construction of drug-target-pathway network
Logged in to Cytoscape 3.9.1 software (https://cyto-scape.org/) to import the network file and typed file of SA L-core target-pathway respectively, to construct the "drug-target-pathway" network diagram and beautified it with Layout and Style tools.

Molecular docking

PDB ID (protein data bank ID)
PDB ID: 5IAS (Caspase-3, RCSB PDB). PDB ID: 5FUQ Chain A (NQO1, RCSB PDB). PDB ID: 3K1W Chain A (REN, RCSB PDB). PDB ID: 5EDU (HDAC6, RCSB PDB). PDB ID: 6H5W (ACE, RCSB PDB). PDB ID: 8BF1 (PPARγ, RCSB PDB). PDB ID: 6GL8 (BCL2, RCSB PDB). PDB ID: 2SRC (SRC, RCSB PDB). PDB ID: 5UUI (TNF, RCSB PDB). PDB ID: 5BUO (APP, RCSB PDB). PDB ID: 4BKX Chain B (HDAC1, RCSB PDB). PDB ID: 8OXQ Chain A (ATM, RCSB PDB).

Protein preprocessing
The crystal structures of the 14 proteins were obtained by the *RCSB PDB* database (https://www.rcsb.org/). The protein preparation wizard module in Schrodinger software was used to process the obtained protein crystals (protein preprocess, regenerate states of native ligand, H-bond assignment optimization, protein energy minimization, and removal waters).

Ligand preprocessing
The 2D sdf structure file of salidroside was processed by the LigPrep module in Schrodinger and all its 3D chiral conformations were generated.

Active site recognition
The SiteMap module in Schrodinger was used to predict the best binding site. Then, the most appropriate Enclosing box was set in the Receptor Grid Generation module of Schrodinger to perfectly wrap the predicted binding sites, obtaining the active sites of 14 proteins.

Molecular docking
Schrodinger Maestro 13.5 (February 2023 version) was used to perform molecular docking of the treated SAL with the active sites of 14 proteins respectively (XP docking with the highest precision). The lower the score corresponds lower the binding free energy of SAL and proteins and the higher the binding stability.

Molecular mechanics generalized born surface area (MM-GBSA) analysis
According to the MM-GBSA analysis of the SAL and the active sites of 14 proteins, MM-GBSA dG Bind can approximately represent the binding free energy between small molecules and proteins. The lower the binding free energy, the higher the binding stability of the ligand compound to the protein.

Molecular dynamics simulation
To further optimize the binding mode of compound-protein complexes, we performed conventional molecular dynamics simulations by using the Desmond program. The OPLS4 force field was employed to parameterize the protein and small molecules, while the SPCE model was used for the water solvent. The protein-small molecule complex was placed in a cubic water box and solvated. The system's charge was neutralized by adding 0.150 M chloride and sodium ions. The energy of the system was initially minimized by using the steepest descent minimization method for 50,000 steps. Subsequently, the positions of heavy atoms were restrained for NVT and NPT equilibration for an additional 50,000 steps. The system temperature was maintained at 300 K and the system pressure was maintained at 1 bar. After completing the two equilibration stages, an unrestricted simulation was performed for 100 ns. The interactions were analyzed, and dynamic trajectory animations were generated using Maestro 13.5.

Saturation mutagenesis

Crystal selection
Following flexible XP docking of SAL with Caspase-3 proteins, MM-GBSA-optimized complex crystals served as the research object for this saturation mutagenesis.

Selection of saturation mutagenesis sites
Based on the previous work, 4 amino acids interacting with SAL on Caspase-3 protein were selected as Saturation mutagenesis sites (TRP206, ASN208, GLU246, PHE250). The Residue Scanning module in Schrodinger was adopted to set the amino acids at each site as all possible mutations (20 in total), and then the optimization model was set as Side-chain prediction with backbone minimization. All possible mutations were then performed on all sites.

Affinity calculation
The affinity of Caspase-3 proteins to SAL was evaluated by the affinity parameter. The Caspase-3 proteins in the complex were set as system A and the SAL ligand was set as system B. The parameters of system A and system B were calculated. Executed the Python command: $SCHRODINGER/run residue_scanning_backend.py.

Visualization of saturation mutation results
The Residue Scanning Viewer was utilized to merge and sketch the findings displaying a line graph depicting the ΔAffinity values in ascending order.

Surface plasmon resonance analysis
Biacore T200 and 1 K (GE Healthcare, USA) were used for real-time binding interaction studies. The theoretical isoelectric point of Caspase-3 protein was about 6.09, and it was intended to be fixed by the amino coupling method. In this study, the amino coupling method of the CM5 chip (Lot: 10,342,920) was used to fix the Caspase-3 protein to the Fc2 channel, and the Fc1 channel was used as the reference channel for activation-blocking treatment. The conditions of Caspase-3 protein coupling were as follows: the concentration of Caspase-3 protein was about 60 μg/mL, the system contained sodium acetate solution pH4.0, the activation time was 420 s, and the sealing time was 420 s. SAL was diluted with 1.0 × PBS-P + solution (pH 7.4) containing 5% DMSO into control solutions with concentrations of 250, 125, 62.5, 31.25, and 15.63 μmol/L. The positive drug Z-DEVD-FM was diluted into positive control solutions with concentrations of 250, 125, 62.5, 31.25, and 15.63 μmol/L with 1.0 × HBS-P + solution (pH 7.4) containing 5% DMSO. The conditions for the determination of SAL were as follows: the injection time was 60 s, the dissociation time was 60 s, the flow rate was 30 μL/min and there was no regeneration. The conditions for the determination of Z-DEVD-FMK were as follows: injection time of 60 s, dissociation time of 60 s, flow rate of 30 μL/min, and no regeneration.

Western blot analysis (WB)
The different protein levels in the gastrocnemius tissue were detected by WB. The tissues were lysed with RIPA buffer containing 1 mM protease inhibitor, and 1 mM phosphatase inhibitor and collected using a cell scraper. Total tissue protein was extracted and protein concentration was determined using the BCA protein assay kit (Beyotime Biotechnology, Jiangsu, China). An equal amount of cell lysate was separated on a 10% SAL-polyacrylamide gel and transferred to a tailored polyvinylidene fluoride (PVDF) membrane according to the size of the protein. Then the membrane was blocked with Tris-buffered Tween 20 (TBST) with 5% non-fat dry milk at 25 °C for 2 h. Subsequently, the membrane was incubated with the following primary antibodies overnight at 4 °C: Anti-Cleaved-Caspase-8 Rabbit pAb (1:5000), Anti-Caspase-8 p18 Rabbit pAb (1:5000), Anti-Cleaved-Caspase-3 Rabbit pAb (1:5000), Anti-Caspase-3 P17 Rabbit pAb (1:5000), Anti -PARP1 Rabbit pAb (1:5000), Anti-PARP1 p85 Rabbit pAb (1:5000) and Anti-beta Actin Rabbit pAb (1:5000). Then, the membrane was washed with TBST three times, and incubated the PVDF membrane with goat anti-rabbit secondary antibodies (1:3000) at 25 °C for 2 h. Finally, the target protein was detected by an enhanced chemiluminescence system (Boster, China). Densitometric values of protein bands were quantified by Image J software.

Statistical analysis
All data were presented as Mean ± SD. Data were analyzed using GraphPad Prism™ software 5.0 (GraphPad Software, Inc. California, USA). One-way analysis of variance (ANOVA) followed by a Dunnett's post-test was used to determine the difference between the groups. All groups are compared with the Model group, * $P < 0.05$, ** $P < 0.01$, *** $P < 0.001$.

Discussion
Rhodiola rosea is often used in traditional Chinese medicine to treat diabetes. Its specific substance is SAL, which facilitates the function of nerve repair and anti-muscular atrophy. Therefore, SAL has a very high potential to ameliorate DA[6,8]. The activity of SAL in alleviating DA was determined using STZ-induced diabetic rat models. It can reduce blood glucose levels and gastrocnemius fibrosis, while augmenting body weight, front paw tension, and average muscle fiber area. Compared with the control group, the expression level of MyoG was significantly ($P < 0.001$) decreased in the model group, while the expression level of FBXO32 was significantly ($P < 0.001$) increased, which could be reversed after 4 weeks of salidroside treatment ($P < 0.001$, Fig. 1F and G). MyoG mediates muscle production, and FBXO32 is a marker of muscle atrophy. Therefore, the IHC results also indicate that SAL can alleviate DA. The result indicates that SAL has a good ability to relieve DA, but its specific mechanism is not clear. There were different explanations for the pathogenesis of DA. For example, lumbosacral root, nerve plexus, and peripheral neuropathy lead to muscle atrophy[23]. Insulin plays an important role in the anabolic process of skeletal muscle, and impaired insulin action may lead to decreased protein synthesis and increased degradation, resulting in decreased muscle mass[24]. Similarly, diabetic muscular atrophy is associated with an increase in inflammatory cytokines[25]. Large vascular complications, namely peripheral vascular diseases may lead to muscle atrophy by inducing muscle ischemia[26]. Ultimately, these mechanisms can be summarized as imbalances in myocyte protein synthesis and degradation leading to muscle atrophy. In order to explore the potential mechanism, network pharmacology, molecular docking, molecular dynamics simulation, and other methods were used to predict the potential mechanism of SAL ameliorating DA.

61 targets of SAL ameliorating DA were discovered through network pharmacology and 14 core targets (TNF, APP, Caspase-3, PPARγ, NQO1, HDAC1, BCL2, SRC, HDAC6, ACE, MAPK3, HSP90AA1, ATM, and REN) were screened by constructing PPI network. Molecular docking is a technique that has been widely used in drug development based on computational structural analysis. Among them, the XP mode is flexible docking (both protein and ligand are flexible) and it is also the most detailed calculation mode that could be used for

molecular docking calculation with higher resolution for specific targets[27]. XP docking results need to refer to XP Gscore, which is generally believed to be less than −6 indicating that the ligand and protein have stable binding properties. The value of MM-GBSA energy is lower than −30 kcal/mol, indicating that the ligand binds to the protein stably[28]. SAL and Caspase-3 had the best docking performance with a docking score of −10.76, and the result of MM-GBSA was −47.34 kcal/mol. With low binding free energy and the extremely low value of docking score, it could be indicated that the combination of SAL and Caspase-3 was stable. Therefore, this study identified Caspase-3 as a SAL potential target for ameliorating DA.

Apoptosis or programmed cell death is a cellular mechanism used to eliminate cells that have been injured, infected, or have reached the end of their lifespan[29]. The triggering of apoptosis is mainly achieved through mitochondrial dysfunction, endoplasmic reticulum stress, and activation of death receptors, which induce cell shrinkage, nuclear fragmentation, and the production of apoptotic bodies, ultimately leading to cell death. These processes are strictly regulated by the proteases of the Caspases family which usually exist in healthy cells as inactive precursors and are activated during the process of apoptosis[30]. Among them, caspase3 is the core executor of apoptosis and holds an irreplaceable key position in the apoptotic signaling pathway, responsible for completing the biochemical and morphological changes of programmed cell death.

Caspase-3 protease can cleave and inactivate proteins that are essential for maintaining cytoskeleton, DNA repair, signal transduction, and cell cycle control, and is an important mediator and recognized biochemical index mediating apoptosis[31]. The degradation of myocyte protein can be significantly enhanced by the increase of apoptosis. The ubiquitin–proteasome system is a key proteolytic pathway activated during skeletal muscle atrophy[32]. The majority of the structural proteins in myocytes were found within actinomyosin complexes and myofibrils. However, the proteasome was incapable degrade these intact complexes[33]. Caspase-3 has been shown to degrade actinomyosin complexes in vitro with the resulting fragment subsequently degraded by the 26S proteasome which suggested that Caspase-3 activation and subsequent actin cleavage were key initial steps in muscle atrophy[33]. High glucose could cause oxidative stress in many cell types and activate apoptosis-related proteins such as Caspase-3. Therefore, targeting Caspase-3 has significantly high therapeutic potential for ameliorating DA[34]. SPR results showed that SAL and Caspase-3 can bind specifically.

To verify that SAL directly targets caspase3 to exert its anti-DA activity, we also detected the expression of the upstream proteins and substrates of caspase3. WB results revealed that salidroside alleviated DA by inhibiting the activity of Caspase-3 protease independently of Caspase8 protease, suggesting that salidroside directly targeted Caspase-3 protease to inhibit apoptosis pathway and alleviate DA. SAL can inhibit cell apoptosis induced by Caspase-3 activation[35–37]. In addition, SAL can inhibit denervated skeletal muscle atrophy, which also proves the feasibility of SAL targeting Caspase-3 to ameliorate DA[38]. The main amino acids that played an important role in the binding of SAL and Caspase-3 protein were TRP206, ASN208, TRP214, and PHE250, and their interactions were mainly water bridge, hydrogen bond, and hydrophobic. Caspase-3 recognized substrate-cutting sites through three highly conserved residues of the Caspase family named ARG64, GLN161, and ARG207[39,40]. The amino acids that played an important role in the binding of SAL and Caspase-3 protein mainly included TRP206 and ASN208, which were located around the active site ARG207. At present, the design strategy around the active site can also improve the selectivity and potency of drugs, reduce adverse reactions, and improve the therapeutic effect. Among the top10 Δaffinity results of the Caspase-3 protein, 206 sites appeared more frequently, which can be further verified in the future.

Conclusion

This study verified the activity of salidroside in alleviating DA in an STZ-induced diabetic rat model. Then, Caspase3 was screened out as a potential target of salidroside by using network pharmacology and computational biology, and its binding activity was verified by SPR. Finally, the caspase3-related signaling pathways were detected and it was speculated that salidroside might alleviate DA by inhibiting the apoptotic pathway. We will continue to explore the binding domain of Caspase3 and SAL to provide a theoretical basis for the research and development of anti-DA drugs.

Data availability

The datasets used and analyzed during the current study are available from the corresponding author upon reasonable request. Also, the datasets generated during the current study and Supplementary Information are available in the [Figshare] repository, [https://doi.org/10.6084/m9.figshare.25853599].

Received: 11 April 2025; Accepted: 18 July 2025
Published online: 26 July 2025

References

1. Sun, H. et al. IDF diabetes atlas: Global, regional and country-level diabetes prevalence estimates for 2021 and projections for 2045. *Diabetes. Res. Clin. Pract.* **183**, 109119 (2022).
2. Li, Y. et al. Prevalence of diabetes recorded in mainland China using 2018 diagnostic criteria from the American diabetes association: national cross sectional study. *BMJ* **369**, m997 (2020).
3. Aluganti Narasimhulu, C. & Singla, D. K. Amelioration of diabetes-induced inflammation mediated pyroptosis, sarcopenia, and adverse muscle remodelling by bone morphogenetic protein-7. *J. Cachexia. Sarcopenia.* **12**, 403–420 (2021).
4. Garland, H. Diabetic amyotrophy. *Br. Med. J.* **2**, 1287–1290 (1955).
5. Feng, L. et al. Prevalence and risk factors of sarcopenia in patients with diabetes: A meta-analysis. *J. Clin. Endocrinol. Metab.* **107**, 1470–1483 (2022).
6. Liu, H. et al. Salidroside promotes peripheral nerve regeneration based on tissue engineering strategy using schwann cells and PLGA: In vitro and in vivo. *Sci. Rep.* **12**, 9755 (2022).

7. Sun, S. et al. Antioxidant effects of salidroside in the cardiovascular system. *Evid. Based. Complement. Alternat. Med.* **2020**, 9568647 (2020).
8. Zhang, D. et al. Salidroside mitigates skeletal muscle atrophy in rats with cigarette smoke-induced COPD by up-regulating myogenin and down-regulating myostatin expression. *Biosci. Rep.* **39**, BSR20190440 (2019).
9. Lang, F. et al. Dynamic changes in the mouse skeletal muscle proteome during denervation-induced atrophy. *Dis. Model. Mech.* **10**, 881–896 (2017).
10. Ye, M. et al. Enhanced effects of salidroside on erectile function and corpora cavernosa autophagy in a cavernous nerve injury rat model. *Andrologia* **53**, e14044 (2021).
11. Zhang, R., Zhu, X., Bai, H. & Ning, K. Network pharmacology databases for traditional Chinese medicine: review and assessment. *Front. Pharmacol.* **10**, 123 (2019).
12. Pinzi, L. & Rastelli, G. Molecular docking: Shifting paradigms in drug discovery. *Int. J. Mol. Sci.* **20**, 4331 (2019).
13. Collier, T. A., Piggot, T. J. & Allison, J. R. Molecular dynamics simulation of proteins. *Methods. Mol. Biol.* **2073**, 311–327 (2020).
14. Zheng, J. G., Haseeb, A., Wang, Z. Y. & Wang, H. J. Network pharmacology, computational biology integrated surface plasmon resonance technology reveals the mechanism of ellagic acid against rotavirus. *Sci. Rep.* **14**, 7548 (2024).
15. Zheng, T. et al. Salidroside alleviates diabetic neuropathic pain through regulation of the AMPK-NLRP3 inflammasome axis. *Toxic. Appl. Pharmacol.* **416**, 115468 (2021).
16. Waisundara, V. Y. et al. Baicalin improves antioxidant status of streptozotocin-induced diabetic Wistar rats. *J Agric Food Chem.* **57**, 4096–4102 (2009).
17. Kim, S. et al. PubChem 2023 update. *Nucleic. Acids. Res.* **51**, D1373–D1380 (2023).
18. Musa, I. et al. Formononetin inhibits IgE by huPlasma/PBMCs and mast cells/basophil activation via JAK/STAT/ PI3-Akt pathways. *Front. Immunol.* **15**, 1427563 (2024).
19. Szklarczyk, D. et al. The STRING database in 2023: Protein-protein association networks and functional enrichment analyses for any sequenced genome of interest. *Nucleic. Acids. Res.* **51**, D638–D646 (2023).
20. Xie, R. et al. Identification of core genes and pathways in melanoma metastasis via bioinformatics analysis. *Int. J. Mol. Sci.* **23**, 794 (2022).
21. Kanehisa, M. et al. KEGG for taxonomy-based analysis of pathways and genomes. *Nucleic. Acids. Res.* **51**, D587–D592 (2023).
22. Kanehisa, M. et al. KEGG: New perspectives on genomes, pathways, diseases and drugs. *Nucleic. Acids. Res.* **45**, D353–D361 (2017).
23. Lokhande, K. B. et al. Computational docking investigation of phytocompounds from bergamot essential oil against serratia marcescens protease and fabI: Alternative pharmacological strategy. *Comput. Biol. Chem.* **104**, 107829 (2023).
24. Luan, J. et al. Selectivity mechanism of BCL-XL/2 inhibition through in silico investigation. *Phys. Chem. Chem. Phys.* **24**, 17105–17115 (2022).
25. Dyck, P. J. & Thaisetthawatkul, P. Lumbosacral plexopathy. *Continuum (Minneap Minn).* **20**, 1343–1358 (2014).
26. Grizard, J. et al. Insulin action on skeletal muscle protein metabolism during catabolic states. *Reprod. Nutr. Dev.* **39**, 61–74 (1999).
27. Pillon, N. J. et al. Distinctive exercise-induced inflammatory response and exerkine induction in skeletal muscle of people with type 2 diabetes. *Sci. Adv.* **8**, eabo3192 (2022).
28. Shi, Y. & Vanhoutte, P. M. Macro- and microvascular endothelial dysfunction in diabetes. *J. Diabetes.* **9**, 434–449 (2017).
29. Elmore, S. Apoptosis: a review of programmed cell death. *Toxicol. Pathol.* **35**, 495–516 (2007).
30. Salvesen, G. S. Caspases and apoptosis. *Essays. Biochem.* **38**, 9–19 (2002).
31. Asadi, M. et al. Caspase-3: Structure, function, and biotechnological aspects. *Biotechnol. Appl. Biochem.* **69**, 1633–1645 (2022).
32. Pang, X., Zhang, P., Chen, X. & Liu, W. Ubiquitin-proteasome pathway in skeletal muscle atrophy. *Front. Physiol.* **14**, 1289537 (2023).
33. Du, J. et al. Activation of caspase-3 is an initial step triggering accelerated muscle proteolysis in catabolic conditions. *J. Clin. Invest.* **113**, 115–123 (2004).
34. Wang, J., Yang, H., Wang, C. & Kan, C. Cyp2e1 knockdown attenuates high glucose-induced apoptosis and oxidative stress of cardiomyocytes by activating PI3K/Akt signaling. *Acta. Diabetol.* **60**, 1219–1229 (2023).
35. Fan, H., Su, B. J., Le, J. W. & Zhu, J. H. Salidroside protects acute kidney injury in septic rats by inhibiting inflammation and apoptosis. *Drug. Des. Devel. Ther.* **16**, 899–907 (2022).
36. Cai, L. et al. Salidroside inhibits H2O2-induced apoptosis in PC12 cells by preventing cytochrome c release and inactivating of caspase cascade. *Acta. Biochim. Biophys. Sin.* **40**, 796–802 (2008).
37. Qian, E. W., Ge, D. T. & Kong, S. K. Salidroside protects human erythrocytes against hydrogen peroxide-induced apoptosis. *J. Nat. Prod.* **75**, 531–537 (2012).
38. Wu, C. et al. Salidroside attenuates denervation-induced skeletal muscle atrophy through negative regulation of pro-inflammatory cytokine. *Front. Physiol.* **10**, 665 (2019).
39. Timmer, J. C. & Salvesen, G. S. Caspase substrates. *Cell. Death. Differ.* **14**, 66–72 (2007).
40. Seaman, J. E. et al. Cacidases: Caspases can cleave after aspartate, glutamate and phosphoserine residues. *Cell. Death. Differ.* **23**, 1717–1726 (2016).

Author contributions

H.W. Z.W. and J.Z. designed all the experiments. W.Y. H.W. Z.W. and J.Z. wrote the manuscript. W.Y. and A.H. revised the manuscript. All authors reviewed the manuscript. All authors read and approved the final manuscript.

Declarations

Competing interests

The authors declare no competing interests.

Additional information

Supplementary Information The online version contains supplementary material available at https://doi.org/10.1038/s41598-025-12704-1.

Correspondence and requests for materials should be addressed to J.Z.

Reprints and permissions information is available at www.nature.com/reprints.

Publisher's note Springer Nature remains neutral with regard to jurisdictional claims in published maps and institutional affiliations.